



## Efficient reduction of CO<sub>2</sub> to C<sub>2</sub> hydrocarbons by tandem nonthermal plasma and photocatalysis

He Li, Mengyang Xia, Xiaxin Wang, Ben Chong, Honghui Ou, Bo Lin, Guidong Yang\*

XJTU-Oxford Joint International Research Laboratory of Catalysis, School of Chemical Engineering and Technology, Xi'an Jiaotong University, Xi'an, Shaanxi 710049, China



### ARTICLE INFO

**Keywords:**

Nanoconfined structure  
CO<sub>2</sub> photoreduction  
C<sub>2</sub> hydrocarbons formation  
Nonthermal plasma technology

### ABSTRACT

CO<sub>2</sub> photoreduction to hydrocarbons is a carbon-neutral technology for renewable energy. However, this strategy is challenged by the thermodynamic stability of CO<sub>2</sub> and the low efficiency of multi-photoelectron utilization. In this paper, tandem nonthermal plasma and photocatalysis were used to effectively improve the efficiency of CO<sub>2</sub> reduction to C<sub>2</sub>. We first activated CO<sub>2</sub> by nonthermal plasma technology (NTP) and then converted the activated CO<sub>2</sub> into C<sub>2</sub> products by Cd<sub>0.2</sub>Zn<sub>0.2</sub>S/In<sub>2</sub>O<sub>3</sub> photocatalyst with a special nanostructure. Without the addition of any sacrificial agent, the C<sub>2</sub> yield of the catalyst reached 0.382 μmol h<sup>-1</sup>, which is one of the highest performances to date. In situ experimental and computational studies show that CO<sub>2</sub><sup>+</sup> activated by NTP has higher π orbital and HUMO levels of lone pair electrons and promotes the reduction of CO<sub>2</sub><sup>+</sup> by injecting electrons into the vacant orbital of the active site of Zn. At the same time, the unique structure of Cd<sub>0.2</sub>Zn<sub>0.2</sub>S/In<sub>2</sub>O<sub>3</sub> photocatalyst can extend the life of charge through the optical field enhancement effect, and then react with the CO<sub>2</sub><sup>+</sup> intermediates generated by NTP technology to promote the coupling of C-C bonds, and finally promote the photocatalytic multi-electron reaction to produce C<sub>2</sub> hydrocarbons.

### 1. Introduction

Photocatalytic conversion of CO<sub>2</sub> into multi-carbon fuels is considered one of the potential green ways to ease the pressure on global energy demand [1]. However, the formation of valuable hydrocarbons requires the activation of stable CO<sub>2</sub> (750 kJ/mol) and then undergoes a multi-electron C-C coupling process. At present, the main products of photocatalytic CO<sub>2</sub> reduction reaction are usually C<sub>1</sub>, such as CO, CH<sub>4</sub>, and other products. C<sub>2</sub> hydrocarbons, such as ethylene and ethane, remain challenging. To date, many studies have focused on promoting the yield of multi-carbon products by constructing photocatalysts with multi-electron supply capability and surface active sites to promote the C-C coupling reaction of C<sub>1</sub> intermediates [2]. Although these effective strategies are effective in the generation of C<sub>2</sub> products, the critical step of CO<sub>2</sub> activation is often ignored [3,4]. The product of CO<sub>2</sub> activation can act as a C<sub>1</sub> intermediate to promote the C-C coupling reaction. Therefore, the CO<sub>2</sub> reduction efficiency can be improved more effectively by activating CO<sub>2</sub> first and then reducing it through a photocatalytic reaction.

Non-thermal plasma technology (NTP) is also an effective way to convert CO<sub>2</sub> into high-value-added chemicals [5–7]. The primary

mechanism of NTP consists of creating an electric field by applying a potential difference between parallel plates. Under the action of an electric field, CO<sub>2</sub> gas is easily activated by high-energy electrons to produce short-lived species, such as excited state species, free radicals, electrons, and the long-lived CO and CO<sub>2</sub><sup>+</sup> charged gas at room temperature [8,9]. Although NTP is easy to activate stable CO<sub>2</sub> molecules, there are some limitations, such as the reaction products are mostly C<sub>1</sub> products and low selectivity [10–12]. In addition, the lack of hydrogen protons in the NTP system (pure CO<sub>2</sub> gas) prevented the synthesis of target C<sub>2</sub> hydrocarbon products [13]. Therefore, a potential strategy is to first convert thermodynamically stable CO<sub>2</sub> into more active charged matter (CO<sub>2</sub><sup>+</sup>) through NTP technology, and then reduce activated CO<sub>2</sub> by designing efficient photocatalysts [14]. Accordingly, photocatalysts with multi-electron supply capabilities are essential for realizing the above reaction. This creates extra demands on the photocatalysts, that is, to prolong the photoelectrons' lifetime for CO<sub>2</sub><sup>+</sup> reduction to C<sub>2</sub> products (CO<sub>2</sub><sup>+</sup>+12e<sup>-</sup>→C<sub>2</sub>H<sub>4</sub>+H<sub>2</sub>O; CO<sub>2</sub><sup>+</sup>+14e<sup>-</sup>→C<sub>2</sub>H<sub>6</sub>+H<sub>2</sub>O). Currently, the excitation lifetime timescales for photoelectrons are typically 1–10 ns in bulk photocatalysts and are comparable to the recombination timescale. The multielectron C<sub>2</sub> synthesis process is challenging in such a tiny lifetime of photoelectrons. To solve this conundrum, controlling

\* Corresponding author.

E-mail address: [guidongyang@xjtu.edu.cn](mailto:guidongyang@xjtu.edu.cn) (G. Yang).

the photocatalyst's excited state is critical to enhancing the average excitation lifetime. Many valuable strategies have recently been explored; the most successful ones tend to design nanostructures to achieve the maximum absorption of photons; nanocavity structures provide a great example [15]. The unique structure could promote photoelectrons transition from the ground state ( $S_0$ ) to a higher level ( $S_x$ ), resulting in longer charges' lifetime. At the same time, the long-lived photoelectrons can gather at the metal active sites, reacting with  $\text{CO}_2^+$  produced by NTP to form  $\text{C}_2$  products, ultimately fulfilling the NTP-assisted photocatalytic  $\text{CO}_2$  reduction process [16,17].

In the reported photocatalysts, transition metal-based catalysts (e.g., Cu, Ni, Zn) exhibit high activity, stability and longer electrons lifetimes for  $\text{CO}_2^+$  adsorption and reduction. It is due to the unsaturated coordination (3d or 4 s orbits), more positive Fermi level position, and unique electronic local structure. Among these transition metals, Zinc-based nanomaterials can be used as active centers for photocatalytic CRR. This can be ascribed to the unsaturated 4 s orbit, which can accept electrons on the delocalized  $\pi$  bond of  $\text{CO}_2^+$ . Taken together, the rational design of Zinc-based nanoconfined photocatalysts for NTP-assisted  $\text{CO}_2$  conversion into  $\text{C}_2$  products is essential.

Here, a  $\text{Cd}_{0.8}\text{Zn}_{0.2}\text{S}/\text{In}_2\text{O}_3$  photocatalyst with a unique nanostructure was synthesized by nanostructure engineering. We activated stable  $\text{CO}_2$  to  $\text{CO}_2^+$  using non-thermal plasma technology, and then efficiently converted  $\text{CO}_2^+$  to  $\text{C}_2$  products via this  $\text{Cd}_{0.8}\text{Zn}_{0.2}\text{S}/\text{In}_2\text{O}_3$  photocatalyst. The system provides high  $\text{C}_2$  productivity of  $0.382 \mu\text{mol h}^{-1}$  without any sacrificial agent. In situ experimental and computational studies show that the unique structure of  $\text{Cd}_{0.8}\text{Zn}_{0.2}\text{S}/\text{In}_2\text{O}_3$  photocatalyst can promote the transition of photoelectrons from the ground state ( $S_0$ ) to a higher energy level ( $S_x$ ), and extend the lifetime of charge through optical field enhancement effect [18]. At the same time, long-lived photoelectrons can gather at the metal active site and react with  $\text{CO}_2^+$  intermediates generated by NTP technology to promote the coupling of C-C bonds, and finally promote the photocatalytic multi-electron reaction to produce  $\text{C}_2$  hydrocarbons.

## 2. Experimental section

### 2.1. Chemicals and materials

Indium nitrate ( $\text{In}(\text{NO}_3)_3$ , 99 %), 1, 4-benzenedicarboxylic acid ( $\text{C}_8\text{H}_6\text{O}_4$ , 98 %), N, N-dimethylformamide ( $\text{C}_3\text{H}_7\text{NO}$ , DMF, 99 %), Zinc nitrate ( $\text{Zn}(\text{NO}_3)_2$ , 99 %), Cadmium chloride ( $\text{CdCl}_2$ , 99 %), thioacetamide ( $\text{CH}_3\text{CSNH}_2$ , 99 %). Polyvinylpyrrolidone (PVP, average mol wt 10,000) was purchased from Sinopharm Chemical Reagent Co, Ltd. Ethanol was purchased from Sigma-Aldrich. The deionized water was obtained from a water purification system (OSJ-UP). All the chemical reagents were used as received without further purification.

#### 2.1.1. Synthesis of In-MIL-68 prisms

The In-MIL-68 prisms was synthesized by a solvothermal method. In a typical reaction, 120 mg of  $\text{In}(\text{NO}_3)_3$  and 120 mg of 1, 4-benzenedicarboxylic acid were dissolved in 60 mL of DMF and stirred for 30 min. Then the above solution was transferred in an oil bath at 130 °C for 40 min. After the solution was cooled down to nature temperature, the precipitate was washed with deionized water and ethanol several times and dried at 60 °C for 4 h.

#### 2.1.2. Synthesis of $\text{Cd}_{0.8}\text{Zn}_{0.2}\text{S}$ photocatalysts

In a typical reaction, 0.36 g of  $\text{CdCl}_2$ , 0.04 g of  $\text{Zn}(\text{NO}_3)_2$  and 0.18 g of thioacetamide were dissolved in 60 mL of deionized water and stirred for 30 min. Then the above solution was transferred in an oil bath at 180 °C for 2 h. After the solution was cooled to natural temperature, the precipitate was washed with deionized water and ethanol several times and dried at 60 °C for 4 h, labeled as CZS.

#### 2.1.3. Synthesis of $\text{In}_2\text{O}_3$ solid rods

Typically, the as-obtained In-MIL-68 prisms were annealed in air at 500 °C for 25 min with a heating rate of 4 °C min<sup>-1</sup>, and then the product was washed with deionized water three times, dried in 60 °C for 4 h, labeled as In-1.

#### 2.1.4. Synthesis of nanoconfined $\text{In}_2\text{O}_3$ photocatalysts

Typically, the as-obtained In-MIL-68 prisms were annealed in air at 500 °C for 60 min with a heating rate of 2 °C min<sup>-1</sup>, and then the product was washed with deionized water three times, dried in 60 °C for 4 h, labeled as In-2.

#### 2.1.5. Synthesis of solid $\text{Cd}_{0.8}\text{Zn}_{0.2}\text{S}/\text{In}_2\text{O}_3$ photocatalysts

In a typical procedure, a 200 mg In-1 sample was dissolved in 40 mL deionized water and stirred for 30 min. A certain amount (2 wt%) of  $\text{Zn}(\text{NO}_3)_2$ ,  $\text{CdCl}_2$ , and thioacetamide was added, and the mixture was vigorously stirred for 30 min at room temperature. The mixture was transferred to a 100 mL Teflon-lined stainless-steel autoclave, which was heated to 180 °C for 3 h. When the autoclave was cooled down to room temperature, the mixture was washed with deionized water and ethanol several times, then dried at 60 °C for 4 h, labeled as InCZ-1.

#### 2.1.6. Synthesis of nanoconfined $\text{Cd}_{0.8}\text{Zn}_{0.2}\text{S}/\text{In}_2\text{O}_3$ photocatalysts

In a typical procedure, a 200 mg In-2 sample was dissolved in 40 mL deionized water and stirred for 30 min. A certain amount (2 wt%) of  $\text{Zn}(\text{NO}_3)_2$ ,  $\text{CdCl}_2$  and thioacetamide was added, and the mixture was vigorously stirred for 30 min at room temperature. The mixture was transferred to a 100 mL Teflon-lined stainless-steel autoclave, which was heated to 150 °C for 3 h. When the autoclave was cooled down to room temperature, the mixture was washed with deionized water and ethanol several times, then dried at 60 °C for 4 h, labeled as InCZ-2.

## 2.2. Characterizations

Various instruments were used to measure the experimental products. Transmission electron microscopy (TEM), scanning electron microscopy (SEM), and energy dispersive spectroscopy (EDS) were performed for obtaining TEM, SEM, and EDS maps. A power X-ray diffraction measurement was performed on the samples (Lab X XRD-6100, SHIMADZU) in order to determine their crystal phase. A temperature programmed desorption (TPD, MICROMERITICS AutoChem II 2920) was executed on the as-prepared samples to quantify the adsorption and desorption characteristics of both  $\text{CO}_2^+$  and CO. An electron spin resonance (ESR) analysis, utilizing the Bruker EMX PLUS, was carried out on the CZS and InCZ-2 samples to evaluate the presence of free radicals during photocatalytic reactions. An integrating sphere attachment was used to measure UV-vis diffuse reflectance spectra using a UV-vis spectrophotometer (UV-2600, SHIMADZU). The femtosecond transient absorption spectrum (Helios) was used to measure the ultrafast dynamics of photoexcited charge transfer. An in situ super-resolution confocal microscope (Leica TCS SP8 STED 3X) was used to determine the transient light absorption and fluorescence signal of as-prepared samples. The fluorescence signals of catalysts were measured using an SEM-Raman (Renishaw Raman spectrometer) system and surface-enhanced Raman spectroscopy. Time-resolved fluorescence spectrophotometers (Edinburgh Instruments, FLS980) were used to measure the fluorescence signal and steady-state photoluminescence (PL) spectra at wavelengths of 365 nm and 540 nm. A solid junction apparatus analyzed the surface photovoltage spectra of samples with a light source-monochromator-lock-in detection measurement at 298 K. Data were collected from triple-prism monochromators (Hilger and Watt, D300) with amplification (Brookdeal, 9503-SC). All the surface photovoltage spectra were measured with an ITO electrode film. A Shamrock 750 emission spectrometer obtained the emission spectra. With a CHI660E electrochemical apparatus (Shanghai, China), the electrochemical photocurrent and impedance spectra were measured

using a standard three-electrode cell. This consisted of a working electrode with a platinum wire counter and Ag/AgCl reference electrode. As a working electrode, FTO film was used to test the Mott-Schottky spectra. The electrolyte used in all electrochemical measurements was 1.0 M Na<sub>2</sub>SO<sub>4</sub>. A high-resolution confocal microscope (Leica TCS SP8 STED 3X) was used to obtain super-resolution confocal spectra and images. An inVia Qontor Raman spectrum was used to obtain Raman spectra and mapping data.

### 2.3. In situ FTIR experiment

In situ reaction cells were typically filled with 2 mg of the photocatalyst and purged with CO<sub>2</sub> gas treated by NTP for 1 h. Then 0.2 mL ultra-pure water was added to the reaction cell. An FTIR spectrophotometer Nicolet iS50 was used to carry out the in situ FTIR measurement at room temperature.

### 2.4. In situ Raman experiment

In situ Raman spectroscopy was conducted using Renishaw Raman spectrometers with NTP active CO<sub>2</sub> as the feeding gas. A mixture of 2 mL of ultra-pure water and 10 μL of Nafion solution (10 wt%) was sonicated for 10 min to form a homogeneous solution containing 2 mg of the prepared photocatalysts. The above solution was uniformly coated on a 0.5 × 0.5 cm<sup>2</sup> FTO film and then dried at 60 °C for 12 h to obtain the as-prepared samples for in situ Raman spectroscopy.

### 2.5. FDTD simulations details

Finite-difference time-domain simulations (FDTD) were obtained using Lumerical FDTD Solutions. The geometry of photocatalysts was modeled as hollow hexagonal prisms and solid hexagonal prisms; hollow hexagonal prisms contain clusters inside and hollow hexagonal prisms with particles on the surface. The height of the hexagonal prism was 4 μm, and the refractive index of In<sub>2</sub>O<sub>3</sub> and Cd<sub>0.8</sub>Zn<sub>0.2</sub>S was 1.23 and 1.4, respectively. A normal plane wave illuminated the structure. Along the Y-axis, plane wave polarized light with a wavelength ranging from 200 to 800 nm was used. The mesh override region was set to 0.3 nm for minimum simulation time and maximum field enhancement resolution, and the overall simulation time was 200 fs.

### 2.6. DFT computational details

The plane-wave pseudopotential method depending on density functional theory was used in the first principles calculations. The geometry optimizations and electron structure were adopted by the Vienna Ab initio Simulation Package (VASP), and the electron exchange and correlation potentials were employed by a generalized gradient approximation with the Perdew-Burke-Ernzerhof exchange-correlation functional in VASP code. The van der Waals (vdW) interactions were described using the empirical correction in Grimme's scheme (DFT + D2). Energetics calculations for reaction mechanisms were carried out by using spin-polarized density functional theory (DFT). The A plane-wave cut-off energy of 420 eV was adopted. The heterojunction structure Cd<sub>0.8</sub>Zn<sub>0.2</sub>S/In<sub>2</sub>O<sub>3</sub> is used and the calculation model is composed 127 atoms. Combining with XRD and HRTEM analysis, (101) surface of Cd<sub>0.8</sub>Zn<sub>0.2</sub>S lattice is used as reaction plane. A Monkhorst-Pack 5 × 4 × 1 k-point grid was adopted to sample the Brillouin zone and the vacuum space was 25 Å. Structure optimization calculations were done until the total energy changes were within 1 × 10<sup>-5</sup> eV per atom and the Hellmann-Feynman force on each atomic site was less than 0.05 eV/Å. All Gibbs free energy values were referenced to the computational hydrogen electrode (CHE) model using the proton-coupled electron transfer (PCET) approach. The chemical potential of the H<sup>+</sup>/e<sup>-</sup> pair was considered as half of the H<sub>2</sub> gas molecule. The ΔG value was obtained via the formula: ΔG = ΔE + ΔZPE - TΔS, where ΔE is the reaction

energy difference between the product and reactant occurring on catalysts. ΔZPE and ΔS are the changes in zero point energies and entropy at 298.15 K, which were calculated via considering only the vibrational frequencies.

## 3. Results and discussion

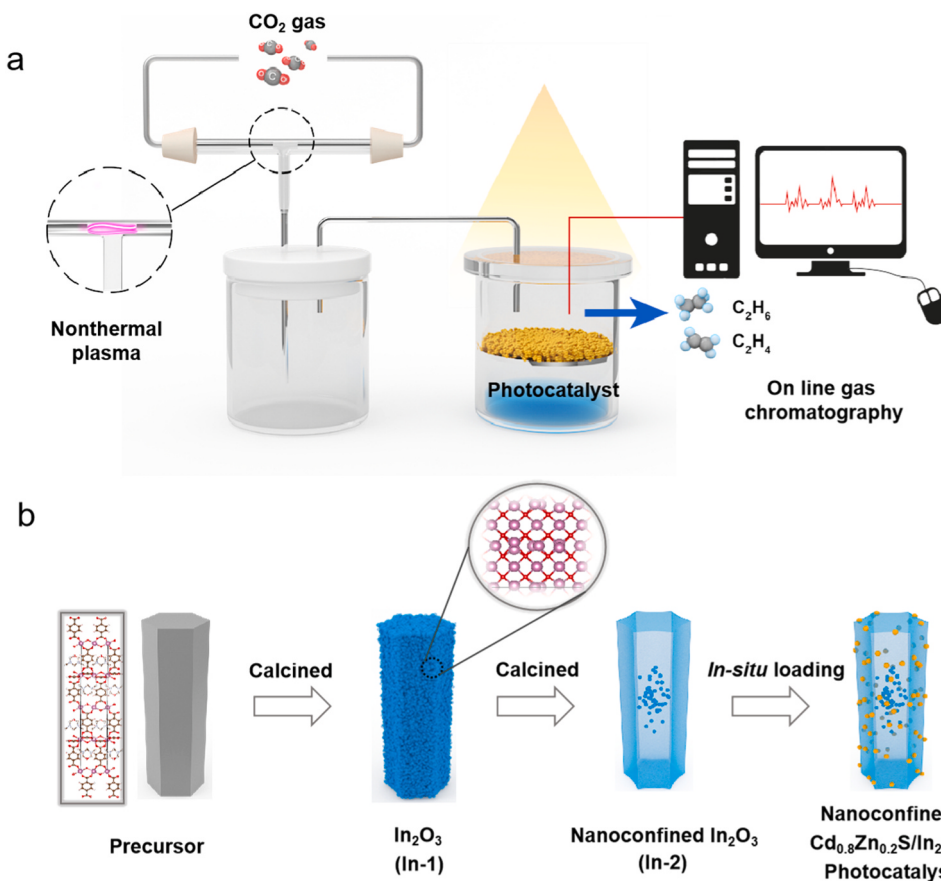
### 3.1. The NTP-assisted photocatalytic CO<sub>2</sub> reaction system and microstructures of photocatalysts

We first proposed to activate CO<sub>2</sub> by coupling a nonthermal plasma process in series integration to generate reactive CO<sub>2</sub><sup>+</sup> to achieve the efficient photocatalytic synthesis of ethane and ethylene (Scheme 1a, Fig. S2, Supporting information). Understanding the pCRR process relies heavily on determining CO<sub>2</sub> products activated by NTP. In situ emission spectra in Fig. S3a detect the gas after the NTP discharge. When high-energy electrons collide with CO<sub>2</sub> molecules, ionization occurs, and a large number of CO<sub>2</sub><sup>+</sup> and CO are produced. To determine the stability of CO<sub>2</sub><sup>+</sup>, according to Fig. S3b, in situ emission spectra indicate that CO<sub>2</sub><sup>+</sup> charge gas can survive for a long time with NTP on. Upon turning off NTP, however, the CO<sub>2</sub><sup>+</sup> signal value will disappear within approximately 190 s (Fig. S3c). Thus, we used an in-situ reaction method to provide CO<sub>2</sub><sup>+</sup> continuously by turning on NTP to activate CO<sub>2</sub> during the photocatalytic reaction. To favour multielectron proton reduction of the CO<sub>2</sub><sup>+</sup> reaction, a nanoconfined Cd<sub>0.8</sub>Zn<sub>0.2</sub>S/In<sub>2</sub>O<sub>3</sub> photocatalyst is rationally developed.

A discussion of the synthesis of photocatalysts is then presented. The In<sub>2</sub>O<sub>3</sub> nanorod (labeled as In-1, Fig. S4) is prepared with the In-based organic framework nanocrystal in Fig. 1a. Afterward, the precursor is calcined in air to obtain a hollow In<sub>2</sub>O<sub>3</sub> nanorod with a cluster inside (labeled as In-2, Fig. S5). In-situ loading a 2 wt% Cd<sub>0.8</sub>Zn<sub>0.2</sub>S on the surface of In<sub>2</sub>O<sub>3</sub> nanorod to obtain the nanoconfined photocatalyst (labeled as InCZ-2, Scheme 1b). In Fig. S6, pure Cd<sub>0.8</sub>Zn<sub>0.2</sub>S and Cd<sub>0.8</sub>Zn<sub>0.2</sub>S/In<sub>2</sub>O<sub>3</sub> bulk material is also synthesized for comparison with the nanoconfined photocatalyst (labeled as CZS and InCZ-1). Scanning electron microscopy (SEM), transmission electron microscopy (TEM), and scanning transmission electron microscopy (STEM) images of InCZ-2 are shown in Fig. 1b, c and Fig. S7. The InCZ-2 photocatalyst has the structure of a hollow hexagonal prism, and the nanocluster is seen clearly to be encapsulated in the internal cavity. The Cd<sub>0.8</sub>Zn<sub>0.2</sub>S nanoparticles are uniformly anchored outside the In<sub>2</sub>O<sub>3</sub> surface. Subsequently, a high-resolution TEM image (HRTEM) exhibits that InCZ-2 has a heterojunction structure (Fig. 1d). The crystallized inner materials with a lattice space of 0.292 nm correspond to the (222) facet of In<sub>2</sub>O<sub>3</sub> [19]. The outside nanoparticle crystal planes can be studied using high-angle annular dark-field scanning transmission electron microscopy (HAADF-STEM). As shown in Fig. 1e, the lattice size of nanoparticles can match 0.316 nm, corresponding to the (101) crystal plane of Cd<sub>0.8</sub>Zn<sub>0.2</sub>S. The formation of InCZ-2 is further confirmed by X-ray diffraction (XRD) in Fig. 1f. The distribution of In, Cd, Zn S, and O elements is examined by an energy-dispersive spectrometer (EDS) mapping and X-ray photoelectron spectroscopy (XPS) in Fig. 1g, Fig. S8 and Table S1.

### 3.2. The characterization of energy band structure and NTP-assisted photocatalytic CO<sub>2</sub> reduction performance

A common goal among researchers is the development of valuable C<sub>2</sub> products using as-prepared photocatalysts. As part of a solar-driven reduction process, photoexcited electrons in a photocatalyst's conduction band (CB) can convert CO<sub>2</sub> into C<sub>2</sub> carbonaceous fuels. That is to say, the conduction band position of as-prepared photocatalysts is crucial to photosynthesize C<sub>2</sub> products. It can be seen from Fig. S9 that the energy gap between In<sub>2</sub>O<sub>3</sub> and Cd<sub>0.8</sub>Zn<sub>0.2</sub>S is 2.32 and 2.0 eV, respectively. Besides, a flat band potential (V<sub>fb</sub>) for In<sub>2</sub>O<sub>3</sub> is estimated to be −0.40 eV, while that for Cd<sub>0.8</sub>Zn<sub>0.2</sub>S is estimated to be −0.35 eV



**Scheme 1.** a) NTP-assisted photocatalytic CO<sub>2</sub> reduction process. b) Schematic illustration of the fabrication of nanoconfined Cd<sub>0.8</sub>Zn<sub>0.2</sub>S/In<sub>2</sub>O<sub>3</sub> photocatalyst.

(Fig. S10). From the semiconductor energy gap formula ( $E_g = VB_{\text{Valence}} - V_{fb}$ ), we can deduce that In<sub>2</sub>O<sub>3</sub> and Cd<sub>0.8</sub>Zn<sub>0.2</sub>S exhibit VB values of 1.92 and 1.65 eV, respectively. Photoexcited electrons are transferred to the Cd<sub>0.8</sub>Zn<sub>0.2</sub>S surface for CO<sub>2</sub> reduction. Thus, the CB photoelectrons of Cd<sub>0.8</sub>Zn<sub>0.2</sub>S can reduce CO<sub>2</sub> into C<sub>2</sub>H<sub>4</sub> and C<sub>2</sub>H<sub>6</sub>, according to the photocatalytic reduction potential diagram (Fig. S11).

Our immediate concern is whether the nanoconfined catalysts exhibit the high NTP-assisted photoreduction activity of CO<sub>2</sub>. In the first step, we use the In-2 catalyst to test the yields of ethylene and ethane at different plasma voltages. Fig. S12a illustrates that the In-2 catalyst exhibits the maximum activity for the C<sub>2</sub> product when the plasma voltage is 50 V, and its activity gradually declines with increasing voltage. This may indicate that under high voltage, the high energy electrons in the plasma electric field are more likely to react inversely with CO<sub>2</sub><sup>+</sup> and change back to CO<sub>2</sub> gas (e<sup>-</sup>+CO<sub>2</sub><sup>+</sup>→CO<sub>2</sub>), resulting in a significant decrease in subsequent photocatalytic activity. Moreover, we investigated the effect of different discharge tip distances on the photocatalytic activity. Fig. S12b illustrates that when the discharge tip distance is 2 mm, the residence time of CO<sub>2</sub> gas in the plasma action area is shortened, resulting in a lower concentration of CO<sub>2</sub><sup>+</sup> and, consequently, a lower photocatalytic activity. With an increase in tip distance to 4 mm, plasma interaction intensity increases, exhibiting photocatalytic performance. However, as the tip distance increases to 6 mm, inert CO<sub>2</sub> cannot effectively activate, causing CO<sub>2</sub> photocatalytic activity to decrease. Therefore, the photocatalytic CO<sub>2</sub> reduction activity was then tested under 50 V plasma voltage and 4 mm discharge tip distance for the other prepared samples.

As a first step, we examined the pCRR activity of photocatalysts without nanostructures under NTP conditions. As shown in Fig. 2a, the InCZ-1 sample shows the great performance in delivering C<sub>2</sub> hydrocarbons rates of 0.219 μmol h<sup>-1</sup>, which are 3.8 and 2 times that of the CZS

and In-1 samples. As shown above, the addition of Cd<sub>0.8</sub>Zn<sub>0.2</sub>S (CZS) to In<sub>2</sub>O<sub>3</sub> significantly enhanced pCRR's performance. There is, however, still a low level of C<sub>2</sub> product activity. Thus, we assessed the pCRR activity of photocatalysts in nanoconfined structures. As expected, the InCZ-2 sample exhibited better pCRR performance with a high C<sub>2</sub> hydrocarbons-evolution rate of 0.382 μmol h<sup>-1</sup> (Fig. 2b). It should be noted that the InCZ-2 sample can maintain C<sub>2</sub>H<sub>4</sub> and C<sub>2</sub>H<sub>6</sub> selectivity at 15.4 % and 82.6 %, respectively (Fig. S13a, b). Nevertheless, there was a significant reduction in the selectivity of the photocatalytic C<sub>2</sub> products produced by the In-2 sample (7.2 % for C<sub>2</sub>H<sub>4</sub> and 47.8 % for C<sub>2</sub>H<sub>6</sub>). It could be attributed to different active sites on the photocatalysts, which can impact adsorption and desorption, as well as reaction intermediates. In addition, the InCZ-2 sample produced oxygen during the pCRR process with NTP assistance (Fig. S13c). As is evident from the above results, the nanoconfined structure photocatalyst is indeed capable of promoting the generation of C<sub>2</sub> products. Furthermore, the pCRR stability test for the InCZ-2 sample is conducted under the same experimental conditions, which reveals a slight decrease in activity over 5 cycles due to washing the photocatalyst after each cycle (Fig. 2c). After cycle-run experiments, the SEM image and XRD pattern of the InCZ-2 sample maintains the original morphology and the main characteristic peaks (Fig. S14). This may be attributed to the special structure of the InCZ-2 sample, in which photogenerated holes react with hydroxyl groups (OH<sup>-</sup>) in the photocatalytic reaction, resulting in the formation of hydroxyl radicals (·OH), which are combined to produce hydrogen peroxide, and then decompose to produce O<sub>2</sub> during the photocatalytic reaction. During this process, photocorrosion of InCZ-2 sample can be greatly suppressed by this process. For the purpose of proving the validity of the above mechanism, we conducted a capture experiment of in situ hydroxyl radicals. As shown in electron spin resonance (ESR) spectra (Fig. S15), a characteristic quartet of peaks (1:2:2:1) associated

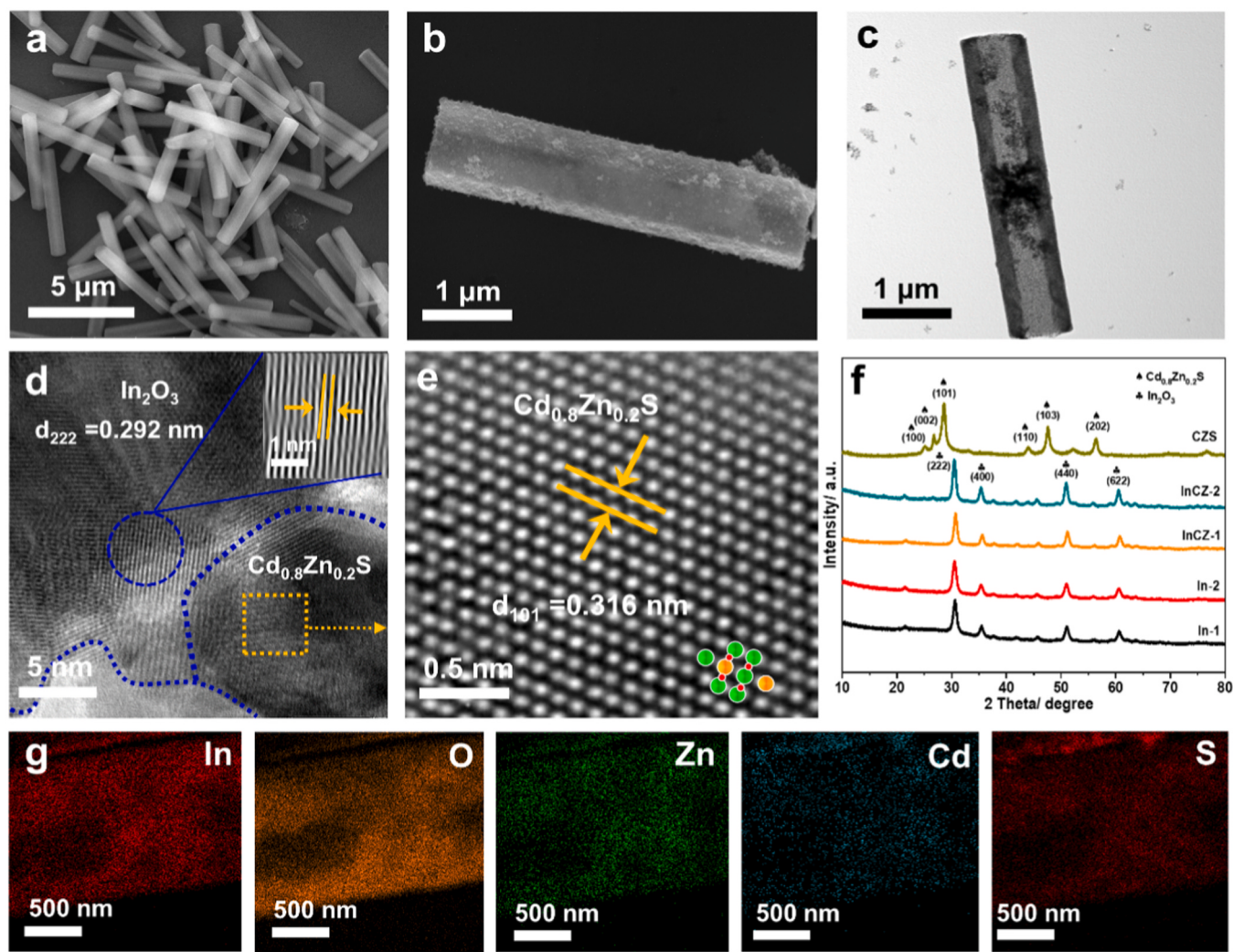


**Fig. 1.** a) SEM image for MIL-68 template. b, c) SEM and TEM images for InCZ-2. d) high-resolution TEM image for InCZ-2 (inset, the selected area electron diffraction pattern). Atom key: Cd (green), Zn (orange), S (red). e) Aberration-corrected HAADF-STEM image for (101) crystal plane of InCZ-2. f) XRD patterns for as-prepared samples. g) EDS mapping results for InCZ-2.

with the 5,5-dimethyl-1-pyrroline-N-oxide-OH (DMPO-OH) radical adduct is immediately detected after 80 s light irradiation. ESR results indicate that the InCZ-2 sample can generate hydroxyl radicals in the NTP-assisted photocatalytic CO<sub>2</sub> reduction reaction, which is the key intermediate for the formation of O<sub>2</sub>. Conversely, there are no characteristic peaks of hydroxyl radicals for CZS sample, indicating that holes are likely to cause corrosion of the catalysis, resulting in poor photocatalytic stability. These results demonstrate excellent photocatalytic stability for InCZ-2. According to Fig. 2d, the maximum QE% for C<sub>2</sub>H<sub>4</sub> and C<sub>2</sub>H<sub>6</sub> in the InCZ-2 sample is 1.15 % and 1.65 %, which is higher than that of the In-1 sample (0.13 % and 0.46 %). More importantly, we have measured CRR activity under an Ar atmosphere with illumination or under CO<sub>2</sub> plasmas without illumination to exclude C<sub>2</sub>H<sub>4</sub> and C<sub>2</sub>H<sub>6</sub> contaminants. In the above reaction system, neither C<sub>2</sub>H<sub>4</sub> nor C<sub>2</sub>H<sub>6</sub> is detected by gas chromatography, which establishes that there are no C<sub>2</sub> product contaminants (Fig. S16). Besides, as photocatalytic H<sub>2</sub> evolution reaction is a competitive reaction, the same conditions are used to measure it. As shown in Fig. S17, there is no detection of H<sub>2</sub> because only water serves as a proton in the reaction system without any sacrificial agent [20,21]. Furthermore, to eliminate the influence of CO gas after plasma treatment, we also measured the photocatalytic activity of CO or CO<sub>2</sub>/CO mixture as the feeding gas. As shown in Fig. S18, the prepared samples exhibit a low photocatalytic synthesis rate of ethylene and

ethane (within the error range), which indicates that the synthesis of photocatalytic C<sub>2</sub> products cannot be enhanced by a large amount of CO generated by plasma, whereas CO<sub>2</sub><sup>+</sup> is critical to ethylene and ethane synthesis [22,23].

### 3.3. Optical and electrochemical properties

A further understanding of how the nanoconfined structure photocatalyst strengthens the multielectron reduction process. In-situ spectrum and finite-difference time-domain (FDTD) calculations of the as-prepared photocatalysts are conducted. As shown in Fig. 3a and Fig. S19, the surface-enhanced Raman spectroscopy (SERS) mapping test of the InCZ-2 and In-1 samples are compared. At 400 nm excitation wavelength, InCZ-2 exhibits a roughly 2-fold enhancement in SERS signal compared to bulk In-1. This difference could be attributed to the nanocavity structure, and the rough surface exhibits a light field enhancement effect (LFE) [24].

In order to eliminate tablet pressing errors caused by the powdered catalyst. An SEM-Raman system analysis of InCZ-2 and In-1 samples is carried out to determine the effects of nanoconfined structures on LFE (Fig. 3b and Fig. S20). As can be seen, the Raman scattering light signal is gathered on the surface of the nanoconfined InCZ-2 sample and shows a strong Raman signal peak in the range of 350–600 nm wavelength [25],

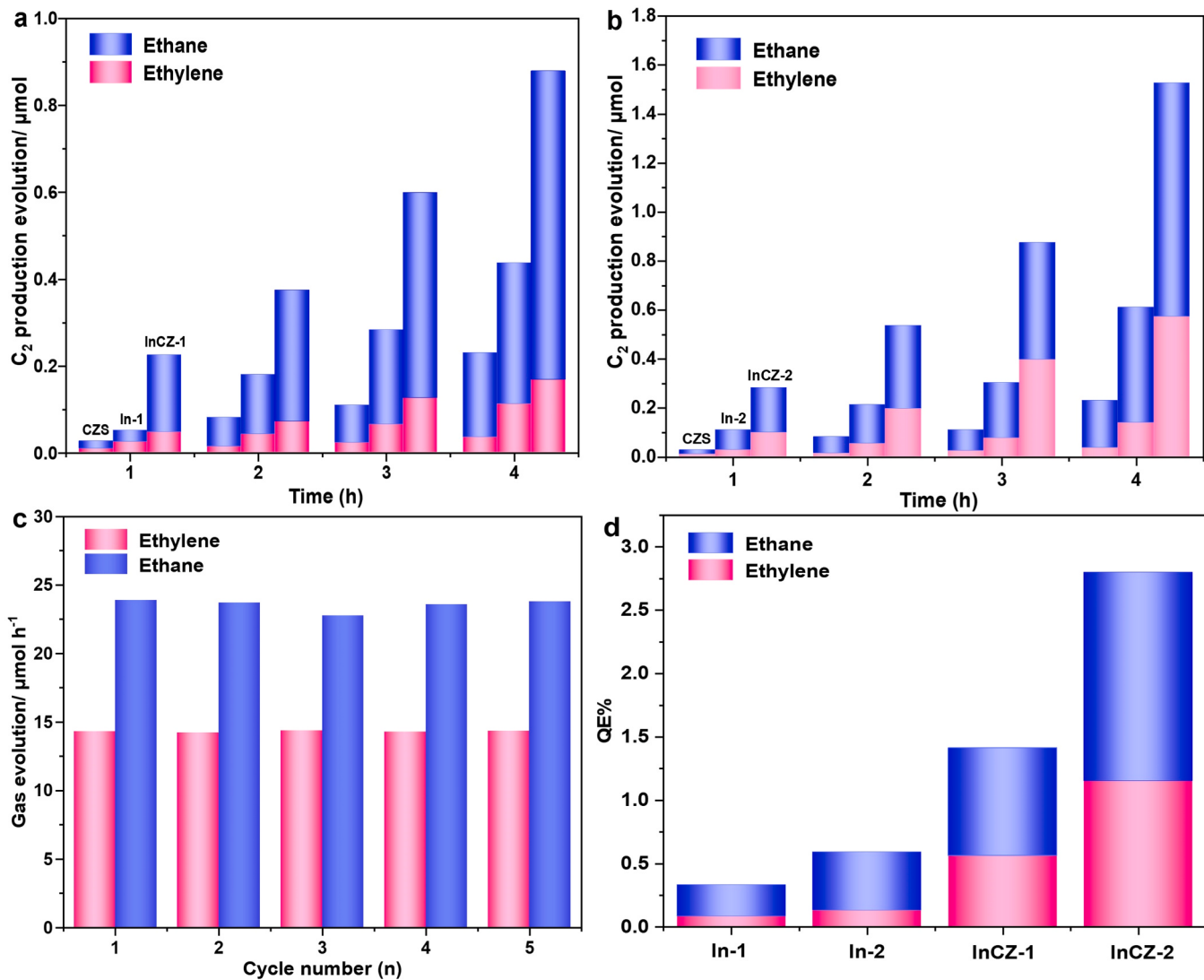


**Fig. 2.** a, b) C<sub>2</sub>H<sub>4</sub> and C<sub>2</sub>H<sub>6</sub> evolution for the as-prepared samples. c) Cycling run test for the InCZ-2 sample. d) Wavelength dependence of the apparent quantum yield for InCZ-2 sample.

[26]. According to the evidence above, the nanocavity and rough surface structure are able to initiate the LFE effect, which enhances light absorption by the catalyst. Further, UV-vis spectroscopy and photoluminescence spectra confirm the above results in Fig. S21 and S22. The aforementioned experimental phenomenon can be verified by FDTD of the as-prepared photocatalysts are simulated (In-1, In-2, InCZ-1, and InCZ-2) [27,28]. For optical simulation, an ellipsometer is used to measure the refractive index of In<sub>2</sub>O<sub>3</sub> and Cd<sub>0.8</sub>Zn<sub>0.2</sub>S (Fig. S23). Through simulation of a catalyst model (InCZ-2) exposed to full light, it can be observed that the light field inside the nanocavity and around the catalyst surface particles is enhanced (Fig. 3c). The bulk (In-1 and InCZ-1) or nanoconfined structure without surface particles (In-2), however, only exhibits a weak light signal on the photocatalyst surface (Fig. S24). As evidenced by spectrum tests and FDTD simulations, the presence of the inner cavity and surface particle structure could increase the near light field to boost light photons absorption of the photocatalyst. When the catalyst absorbs photons, photoelectrons are excited to participate in the multielectron reduction reaction. Thus, photoelectron lifetime plays a critical role in multielectron reduction reactions. For this reason, the fluorescence lifetime of the as-prepared samples is measured using *in situ* super-resolution confocal microscope fluorescence. The In-1 sample only displays a dim fluorescence signal on its surface (Fig. 3d). However, Fig. 3e and Fig. S25 show that the InCZ-2

sample has a regular nanoconfined structure and emits an extremely bright fluorescence signal. Furthermore, transient light absorption spectra with the NTP generator provide additional evidence for this conjecture (Fig. 3f). In a CO<sub>2</sub><sup>+</sup> ion atmosphere, the InCZ-2 sample shows the highest values in transient absorption signals, markedly surpassing the In-1 and In-2 samples by three and two-fold, respectively. Additionally, the light absorption intensity of the InCZ-1 sample loaded with CZS nanoparticles was also improved as compared to the pure In<sub>2</sub>O<sub>3</sub> samples (In-1 and In-2). These experimental results affirm the capacity of nanoconfined structures and heterojunctions to enhance material light absorption efficiency significantly. Also, Fig. 3g provides transient fluorescence spectra (TF) of InCZ-2 and In-1 samples that can be used to calculate the fluorescence lifetimes for comparison. In the short lifetime of excited carriers, it decreases from 1.10 ns (In-1) to 0.039 ns (InCZ-2), while in the long lifetime, it improves from 24.15 to 122.29 ns. In view of this, In-1 and InCZ-2 samples have average fluorescence lifetimes ( $\tau_{avg} = \tau_1 \times rel\% + \tau_2 \times rel\%$ ) of 25.2 and 122.3 ns, respectively (Table S2). The raw data of the TF can be viewed in Fig. S26. Through the above experimental results, structure-induced enhancement of light fields may be responsible for the large increase in fluorescence lifetime. The experimental results described above are in accordance with the results of the FDTD simulation.

To understand why fluorescence lifetime increases, the Femtosecond

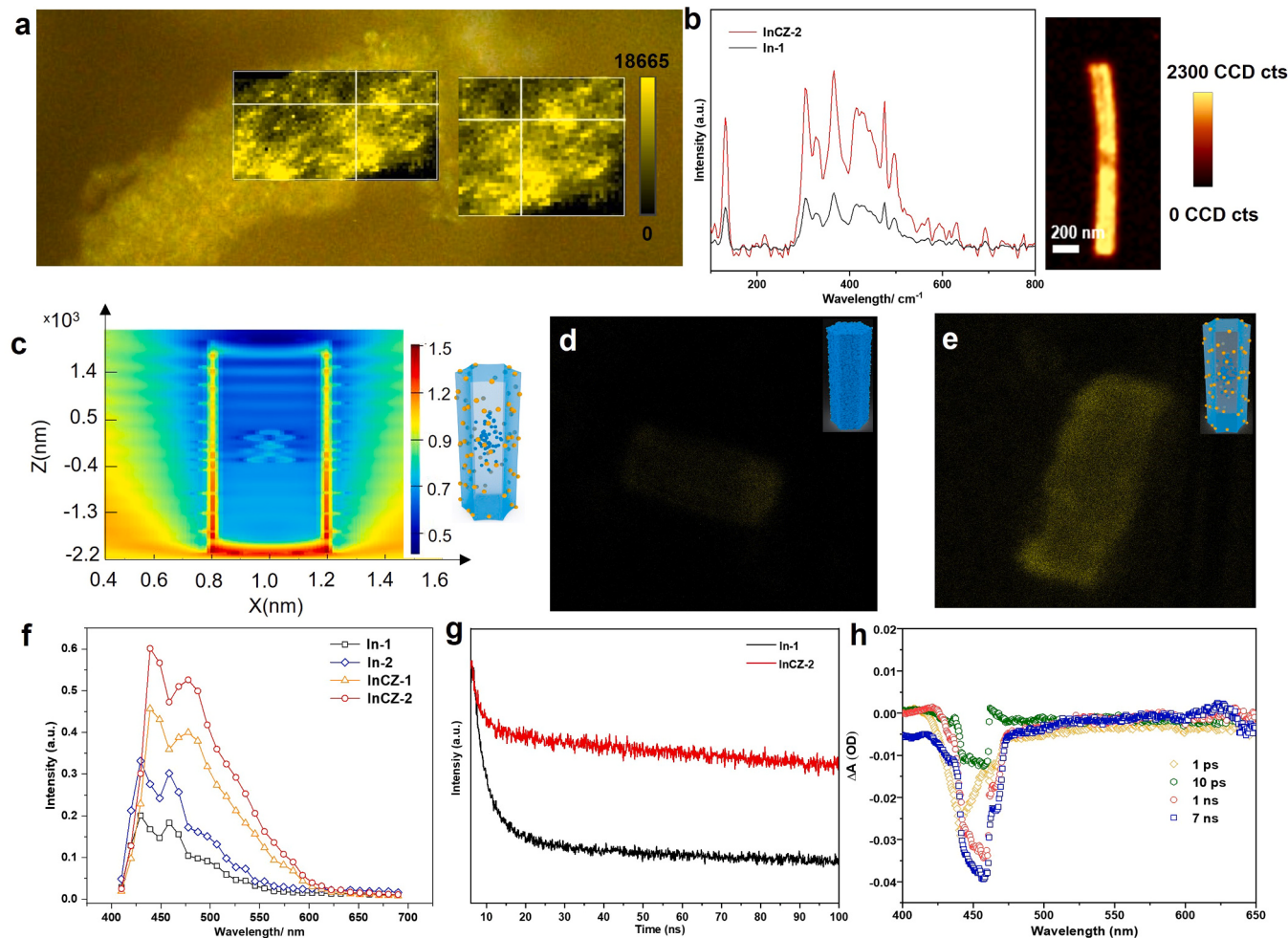


**Fig. 3.** a) SERS mapping test of the InCZ-2 sample. b) The SEM-Raman system analysis of the InCZ-2 and In-1 samples (Inset, the SEM-Raman signal mapping of the InCZ-2 sample). c) FDTD simulation of the InCZ-2 mode. d, e) In situ super-resolution confocal microscope fluorescence of In-1 and InCZ-2 samples. f) Transient light absorption spectra of In-1 and InCZ-2 samples. g) Transient fluorescence spectra of In-1 and InCZ-2 samples. h) Femtosecond transient absorption spectrum of the InCZ-2 sample.

transient absorption spectrum (fs-TA) is measured to monitor the ultrafast dynamics of photoexcited charge transfer. As shown in Fig. 3h and Fig. S27, InCZ-2 exhibits a bleach band peaking at 465 nm due to the 1st excitonic bleach for inner  $\text{In}_2\text{O}_3$ . The shifted bleach band may be due to  $\text{Cd}_{0.8}\text{Zn}_{0.2}\text{S}$  growth on the  $\text{In}_2\text{O}_3$  surface. There is a broad positive absorption band between 475 nm and 650 nm. This may result from the excitonic bleach for  $\text{Cd}_{0.8}\text{Zn}_{0.2}\text{S}$  particles (Fig. S28) [29]. Furthermore, an investigation of transient photocurrent responses is conducted. Fig. S29 shows that the InCZ-2 sample exhibits a more robust photocurrent response than the other samples, indicating that the heterojunction structure could enhance electron-hole separation. According to Fig. S30, the surface photovoltaic spectrum and interface resistance test confirm the same experimental results. Taken together, due to the LFE effect caused by the nano inner cavity and surface particle structure, resulting in a substantial increase in the absorption of light. Moreover, photoelectrons migrate from the inner layer of  $\text{In}_2\text{O}_3$  to the surface of  $\text{Cd}_{0.8}\text{Zn}_{0.2}\text{S}$ , where they relax back to the ground state, greatly extending the life of photoelectrons. This process can prolong photoelectron life and continuously provide electrons in subsequent multielectron reactions.

#### 3.4. Mechanism of photocatalytic $\text{CO}_2$ reduction

Additionally, with  $\text{CO}_2^+$  as the primary reactant, achieving efficient adsorption of  $\text{CO}_2^+$  is a prerequisite for the subsequent multielectron

reduction reaction. Our first approach is to use diffusion reflectance infrared Fourier-transform spectroscopy (DRIFTS) to study the adsorption behavior of the catalysts towards the  $\text{CO}_2^+$ . Fig. S31a shows two bands at 2349.54 and 2353.50  $\text{cm}^{-1}$  associated with the stretching vibration of  ${}^*\text{CO}_2$ . In contrast, when NTP-treated  $\text{CO}_2$  gas is used as the adsorbed gas, the infrared characteristic peaks move in a direction of low wavenumber, and their intensity increases with prolonged adsorption (Fig. S31b). Furthermore, the  $\text{CO}_2^+$  temperature-programmed desorption (TPD) of the as-prepared samples can prove the similar results, as displayed in Fig. S32a. The chemical  $\text{CO}_2^+$  desorption signal strength for the InCZ-2 sample is higher than those of the InCZ-1, In-1, In-2 and CZS samples, indicating that the InCZ-2 sample hints at a potential advantage in efficient  $\text{CO}_2^+$  capture and release. It is noteworthy that CZS exhibits a lower  $\text{CO}_2^+$  desorption temperature, which indicates that pure  $\text{Cd}_{0.8}\text{Zn}_{0.2}\text{S}$  has a weak adsorption of  $\text{CO}_2^+$ . A further test was conducted to determine the performance of the photocatalysts in terms of CO adsorption and desorption. As illustrated in Fig. S32b, all samples exhibit lower CO gas desorption signal peaks as the progressive temperature ramp. In particular, pure CZS and composite samples (InCZ-1, InCZ-2) containing  $\text{Cd}_{0.8}\text{Zn}_{0.2}\text{S}$  show weak CO gas adsorption, indicating limited CO desorption. Accordingly, CO gas is not capable of facilitating photocatalytic  $\text{CO}_2$  reduction to yield  $\text{C}_2$ . The above experimental phenomenon shows that  $\text{CO}_2^+$  can be strongly adsorbed by the active sites on the catalyst surface [30]. Thus, identifying the type and mechanism of active sites can assist us in understanding the mechanism of CRR. Firstly,

we developed the heterostructure of the  $\text{In}_2\text{O}_3$  (222) and  $\text{Cd}_{0.8}\text{Zn}_{0.2}\text{S}$  (101) crystal planes based on the HRTEM and TEM test results (Fig. S33) and screened all possible transition metal active sites (Cd and Zn) on the  $\text{Cd}_{0.8}\text{Zn}_{0.2}\text{S}$  (101) crystal plane by using DFT calculations. As shown in Fig. S34, the Cd atoms in a crystal plane (101) cannot interact with  $\text{CO}_2^+$ , whereas the Zn atoms can interact with  $\text{CO}_2^+$  in a vertical configuration. Adsorption energy ( $E_{\text{ad}} = E_{\text{total}} - (E_{(101)} + E_{\text{CO}_2^+})$ ) refers to the energy released by  $\text{CO}_2^+$  adsorption. In  $\text{Cd}_{0.8}\text{Zn}_{0.2}\text{S}$ ,  $E_{(101)}$  represents the total energy of the (101) crystal plane, while  $E_{\text{CO}_2^+}$  represents the total energy of a relaxed  $\text{CO}_2^+$ . In Fig. S35, the adsorption energy of  $\text{CO}_2^+$  is determined by DFT calculations based on the above formula, which indicates that the Zn active sites of the (101) crystal plane exhibit excellent adsorption properties for  $\text{CO}_2^+$  ( $E_{\text{ad}} = -0.49$  eV).

To further elaborate on the adsorption properties, we compare the orbital resolved pDOS of  $\text{CO}_2^+$  bonding features at Zn sites. As shown in Fig. 4a, the energy levels (3d and 4 s orbits) of Zn in  $\text{Cd}_{0.8}\text{Zn}_{0.2}\text{S}$  (101) are lower than those in  $\text{CO}_2^+$   $\sigma$  orbitals. So, it cannot produce locally occupied d- $\sigma$  (occ) orbitals with adsorbed  $\text{CO}_2^+$ , which is different from the mechanism of traditional transition metal activation. Nevertheless, the energy level of the lone pair electrons and  $\pi$  in the  $\text{CO}_2^+$  is higher than that of the 4 s orbital of Zn, allowing the lone pair electrons and  $\pi$  electrons to be injected into Zn's empty 4 s orbital, forming 2p-4 s and 2-4 s orbital interactions. Thus, it weakens the delocalized  $\pi$  bond in  $\text{CO}_2^+$  and realizes efficient activation of  $\text{CO}_2^+$ . As shown in Fig. 4b, the crystal orbital Hamiltonian population curves (COHP) for  $\text{CO}_2^+$  adsorbed on InCZ-2 are shown as well as the integrated values (ICOHP). More negative ICOHP indicates stronger Zn-\* $\text{CO}_2^+$  coupling. As a result, the electrons in the  $\pi_{(2\text{pz})}$  and lone pair (2 s orbital) of  $\text{CO}_2^+$  have the

strongest interactions with the 4 s empty orbit of Zn (with the highest ICOHP value), whereas the electrons in the 3d orbit of Zn exhibit little interaction [31]. Furthermore, as for  $\text{CO}_2^+$ , lone pairs can donate electrons to the empty 4 s orbital of the reaction sites in Fig. 4b (inset images). These results can be verified by the electron location function and charge density distribution of  $\text{CO}_2^+$  absorption on the  $\text{Cd}_{0.8}\text{Zn}_{0.2}\text{S}$  (101) crystal plane (Fig. S36). In general, the catalytic interaction between  $\text{CO}_2^+$  and the Zn active site is associated with the "acceptance donation" of electrons, where controlling the delocalized  $\pi_{(2\text{pz})}$  orbitals electrons and lone pair electrons of the  $\text{CO}_2^+$  is crucial for accelerating NTP-assisted CRR process.

In situ diffuse reflectance Fourier-transform (DRIFTS) spectroscopy monitors the above reaction process. Fig. 4c shows the in situ (DRIFTS) spectra obtained during the CRR under the NTP condition at increased irradiation times. It is noteworthy that peaks at 1339, 1647 and 1654  $\text{cm}^{-1}$  are assigned to stretching of absorbed \* $\text{OCOOH}$ . The presence of peaks at 1457, 1472, 1507, 1522, and 1541  $\text{cm}^{-1}$  ( $\text{m-CO}_3^2-$ ) is essential evidence of surface-absorbed \* $\text{OCOOH}$  species. Notably, the critical intermediate \* $\text{OCHCHO}$  intensity at 1716  $\text{cm}^{-1}$  increases with increasing irradiation time, signifying  $\text{C}_2$  product formation [32,33]. Moreover, in situ Raman spectroscopy has revealed a peak at 1484  $\text{cm}^{-1}$  that corresponds to the C-O stretching vibration of carboxylate \* $\text{OCH}$  (Fig. S37) [2]. This intermediate is the first step in forming \* $\text{OCHCHO}$ , providing solid evidence to prove the synthesis of  $\text{C}_2$  products. In addition, we conduct a DRIFTS spectrum test of  $\text{CO}_2$  reduction activity without NTP assistance. Only a few reaction intermediates are detected on InCZ-2, suggesting it is difficult for  $\text{CO}_2$  to react with the catalyst to produce  $\text{C}_2$  products (Fig. S38). Based on the above results, it is possible

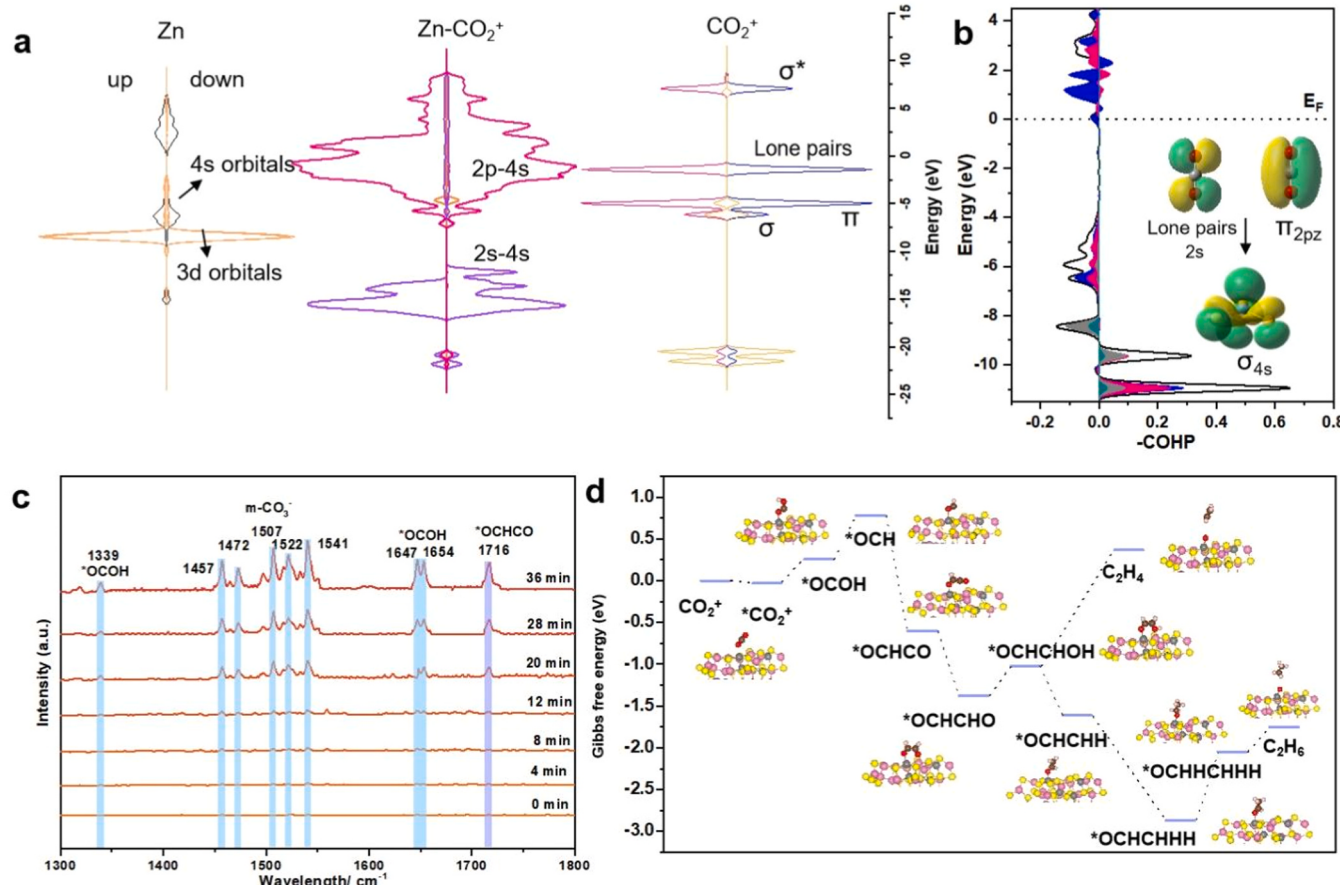


Fig. 4. a) Projected electronic density of states (pDOS) and the orbital distributions of 3d orbitals of Zn active sites, the orbitals of \* $\text{CO}_2^+$  absorbed on Zn active sites and 2p orbitals of  $\text{CO}_2^+$ , respectively. b) COHP analysis of the Zn-O bonding interactions and  $\text{CO}_2^+$  provides electrons to the empty 4 s orbital. c) In situ DRIFT spectra showing the formation of various intermediates over time. d) Gibbs free energy diagrams and  $\text{CO}_2^+$  to  $\text{C}_2\text{H}_4$  and  $\text{C}_2\text{H}_6$  photoreduction pathway on Zn active sites.

to conclude that the CRR process under the NTP condition exhibits excellent performance due to the interaction between  $\text{CO}_2^\ddagger$  and Zn active sites. The Gibbs free energy diagrams calculated by DFT are useful in proving the reaction pathway and intermediate configurations of the NTP-assisted CRR process. Zinc atoms as active sites in the (101) crystal plane can interact with  $\text{CO}_2^\ddagger$  with a vertical absorption configuration (Fig. S39). Fig. 4d illustrates the Gibbs free energy diagrams of NTP-assisted CRR on Zn active sites. In the first step, the  $\text{CO}_2^\ddagger$  on the heterojunction surface is easily activated to generate adsorbed  $^*\text{CO}_2^\ddagger$ , which is subsequently converted uphill into  $^*\text{OCHO}$  and  $^*\text{OCH}$  [34,35]. Afterward, the transition from  $^*\text{OCH}$  to  $^*\text{OCHCO}$  shows a lower uphill energy barrier, indicating that the C-C coupling step has little influence on the reaction. This explains the higher productivity of  $\text{C}_2$  products on InCZ-2 in CRR. Then, the reduction energy barrier from  $^*\text{OCHCO}$  to  $^*\text{OCHCHO}$  is thermodynamically favorable with an energy release of 0.77 eV. With multi-step hydrogenation steps in the pathway, the production of  $\text{C}_2\text{H}_4$  displays the greatest energy barrier ( $\Delta G=1.98$  eV), illustrating the difficulty of desorbing ethylene. However, the production of ethane gas has a  $\Delta G$  of 0.29 eV, which is far lower than ethylene production's energy barrier. Overall, the energy expenditure from  $^*\text{OCHCHOH}$  to  $\text{C}_2\text{H}_4$  is higher than that from  $^*\text{OCHHCHHH}$  to  $\text{C}_2\text{H}_6$ , further verifying the yield ranking of  $\text{C}_2\text{H}_6 > \text{C}_2\text{H}_4$ , which is consistent with the quantum efficiency and pCRR activity results. Taken together, it is evident from these experimental and calculated results synergistically that  $\text{CO}_2^\ddagger$  can be readily activated on Zn sites and that  $\text{C}_2\text{H}_4$  gas desorption is a rate-determining step in the reaction pathway.

#### 4. Conclusion

This work would enrich our knowledge in designing efficient photocatalysts for photocatalytic nitrogen reduction. In summary, a demonstrated photocatalytic  $\text{CO}_2$  conversion into  $\text{C}_2$  products under NTP enables facile  $\text{CO}_2^\ddagger$  absorption and efficient ethylene and ethane production in two-stage synergistic systems. A developed nanoconfined  $\text{Cd}_{0.8}\text{Zn}_{0.2}\text{S}/\text{In}_2\text{O}_3$  photocatalyst with a long photo-electrons lifetime exhibits a significant  $\text{C}_2$  products yield of  $0.382 \mu\text{mol h}^{-1}$ , respectively. Combining a series of in situ measurements and DFT calculations reveals an "acceptance donation" reaction mechanism for NTP-assisted CRR on Zinc-based nanoconfined photocatalysts. A high-energy plasma electric field produces  $\text{CO}_2^\ddagger$ . The 4 s orbits of Zn active sites can accept the lone pair electrons and  $\pi_{(2p_z)}$  orbits electrons of  $\text{CO}_2^\ddagger$ . This brand-new "acceptance donation" phenomenon leads to excellent performance and selectivity for photocatalytic CRR to  $\text{C}_2\text{H}_4$  and  $\text{C}_2\text{H}_6$ . This work provides new insights and opportunities for manufacturing carbon-neutral energy.

#### CRediT authorship contribution statement

**He Li:** Methodology, Investigation. **Mengyang Xia:** Formal analysis. **Xiaxin Wang:** Visualization. **Ben Chong:** Validation. **Honghui Ou:** Investigation. **Bo Lin:** Data curation. **Guidong Yang:** Investigation, Writing-Review & Editing, Supervision, Funding acquisition.

#### Declaration of Competing Interest

The authors declare that they have no known competing financial interests or personal relationships that could have appeared to influence the work reported in this paper.

#### Data availability

Data will be made available on request.

#### Acknowledgements

This work was supported by the National Key R&D Program of China

(2020YFA0710000), Innovation Capability Support Program of Shaanxi (NO. 2023-CX-TD-26), Joint Funds of the National Natural Science Foundation of China (U22A20391), National Natural Science Foundation of China (Grant Nos. 22308272, 22108214), the Key R&D Program of Shaanxi Province (2023-YBGY-323).

#### Appendix A. Supporting information

Supplementary data associated with this article can be found in the online version at doi:10.1016/j.apcatb.2023.123423.

#### References

- [1] J. Albero, Y. Peng, H. García, Photocatalytic  $\text{CO}_2$  reduction to  $\text{C}_2^\ddagger$  products, *ACS Catal.* 10 (2020) 5734–5749.
- [2] J. Duan, T. Liu, Y. Zhao, R. Yang, Y. Zhao, W. Wang, Y. Liu, H. Li, Y. Li, T. Zhai, Active and conductive layer stacked superlattices for highly selective  $\text{CO}_2$  electroreduction, *Nat. Catal.* 13 (2022) 2039–2050.
- [3] X. Feng, R. Zheng, C. Gao, W. Wei, J. Peng, R. Wang, S. Yang, W. Zou, X. Wu, Y. Ji, H. Chen, Unlocking bimetallic active sites via a desalination strategy for photocatalytic reduction of atmospheric carbon dioxide, *Nat. Commun.* 13 (2022) 2146.
- [4] C.H. Cho, C.O. Asperti, M.E. Turk, J.M. Kikkawa, S.W. Nam, R. Agarwal, Tailoring hot-exciton emission and lifetimes in semiconducting nanowires via whispering-gallery nanocavity plasmons, *Nat. Mater.* 10 (2011) 669–675.
- [5] C.H. Cho, C.O. Asperti, J. Park, R. Agarwal, Silicon coupled with plasmon nanocavities generates bright visible hot luminescence, *Nat. Photonics* 7 (2013) 285–289.
- [6] Y.Y. Birdja, E. Pérez-Gallent, M.C. Figueiredo, A.J. Göttle, F. Calle-Vallejo, M.T. M. Koper, Advances and challenges in understanding the electrocatalytic conversion of carbon dioxide to fuels, *Nat. Energy* 4 (2019) 732–745.
- [7] Y. Wu, X.-F. Yu, Y. Du, L. Xia, O. Guo, K. Zhang, W. Zhang, S. Liu, Y. Peng, Z. Li, X. Yang, A combination of two swords thermo-bluelight-synergistic-catalytic  $\text{CO}_2$  cycloaddition on  $\text{ZnIn}_2\text{S}_4$  exposed abundant of Zinc cation sites, *Appl. Catal. B: Environ.* 331 (2023), 122732.
- [8] Y. Ren, C. Yu, L. Wang, X. Tan, Z. Wang, Q. Wei, Y. Zhang, J. Qiu, Microscopic-level insights into the mechanism of enhanced  $\text{NH}_3$  synthesis in plasma-enabled cascade  $\text{N}_2$  oxidation–electroreduction system, *J. Am. Chem. Soc.* 144 (2022) 10193–10200.
- [9] H. Zhang, S. Si, G. Zhai, Y. Li, Y. Liu, H. Cheng, Z. Wang, P. Wang, Z. Zheng, Y. Dai, T.X. Liu, B. Huang, The long-distance charge transfer process in ferrocene-based MOFs with  $\text{FeO}_6$  clusters boosts photocatalytic  $\text{CO}_2$  chemical fixation, *Appl. Catal. B: Environ.* 337 (2023), 122909.
- [10] L. Wang, Y. Yi, C. Wu, H. Guo, X. Tu, Hybrid palladium nanoparticles for direct hydrogen peroxide synthesis: the key role of the ligand, *Angew. Chem. Int. Ed.* 56 (2017) 1679–13683.
- [11] C. Stere, J. Anderson, S. Chansai, J. Delgado, A. Goguet, W. Graham, C. Hardacre, S. Taylor, X. Tu, Z. Wang, H. Yang, Non-thermal plasma activation of gold-based catalysts for low-temperature water–gas shift catalysis, *Angew. Chem. Int. Ed.* 56 (2017) 5579–5583.
- [12] G. Chen, T. Godfroid, N. Britun, V. Georgieva, M.-P. Delplancke-Ogletree, R. Snyders, Plasma-catalytic conversion of  $\text{CO}_2$  and  $\text{CO}_2/\text{H}_2\text{O}$  in a surface-wave sustained microwave discharge, *Appl. Catal. B: Environ.* 214 (2017) 114–125.
- [13] C. Song, X. Han, Q. Yin, D. Chen, H. Li, S. Li, Performance intensification of  $\text{CO}_2$  absorption and microalgae conversion (CAMC) hybrid system via low temperature plasma (LTP) treatment, *Sci. Total Environ.* 801 (2021), 149791.
- [14] S. Chen, W.H. Li, W. Jiang, J. Yang, J. Zhu, L. Wang, H. Ou, Z. Zhuang, M. Chen, X. Sun, D. Wang, Y. Li, MOF encapsulating N-heterocyclic carbene-ligated copper single-atom site catalyst towards efficient methane electrosynthesis, *Angew. Chem. Int. Ed.* 61 (2022), e202114450.
- [15] H. Li, B. Chong, B. Xu, N. Wells, X. Yan, G. Yang, Nanoconfinement-induced conversion of water chemical adsorption properties in nanoporous photocatalysts to improve photocatalytic hydrogen evolution, *ACS Catal.* 11 (2021) 14076–14086.
- [16] B. Ashford, X. Tu, Non-thermal plasma technology for the conversion of  $\text{CO}_2$ , *Curr. Opin. Green Sust. Chem.* 3 (2017) 45–49.
- [17] G. Centi, S. Perathoner, G. Papanikolaou, Plasma assisted  $\text{CO}_2$  splitting to carbon and oxygen: a concept review analysis, *J. CO<sub>2</sub> Util.* 54 (2021), 101775.
- [18] S. Xu, J.C. Whitehead, P.A. Martin,  $\text{CO}_2$  conversion in a non-thermal, barium titanate packed bed plasma reactor: the effect of dilution by Ar and  $\text{N}_2$ , *Chem. Eng. J.* 327 (2017) 764–773.
- [19] Y.X. Pan, Y. You, S. Xin, Y. Li, G. Fu, Z. Cui, Y.L. Men, F.F. Cao, S.H. Yu, J. B. Goodenough, Photocatalytic  $\text{CO}_2$  reduction by carbon-coated indium-oxide nanobelts, *J. Am. Chem. Soc.* 139 (2017) 4123–4129.
- [20] P. Das, T.K. Chini, J. Pond, Probing higher order surface plasmon modes on individual truncated tetrahedral gold nanoparticle using cathodoluminescence imaging and spectroscopy combined with FDTD simulations, *J. Phys. Chem. C* 116 (2012) 15610–15619.
- [21] J.A. Schuller, E.S. Barnard, W. Cai, Y.C. Jun, J.S. White, M.L. Brongersma, Plasmonics for extreme light concentration and manipulation, *Nat. Mater.* 9 (2010) 193–204.

- [22] H. Chen, Y. Mu, Y. Shao, S. Chansai, H. Xiang, Y. Jiao, C. Hardacre, X. Fan, Nonthermal plasma (NTP) activated metal-organic frameworks (MOFs) catalyst for catalytic CO<sub>2</sub> hydrogenation, *AIChE J.* 66 (2020), e16853.
- [23] J. Zheng, C. Wang, W. Chu, Y. Zhou, K. Köhler, CO<sub>2</sub> Methanation oversupported Ru/Al<sub>2</sub>O<sub>3</sub> catalysts: mechanistic studies by *in situ* infraredspectroscopy, *ChemistrySelect* 12 (2016) 3197–3203.
- [24] R.H. Siddique, S. Kumar, V. Narasimhan, H. Kwon, H. Choo, Aluminum metasurface with hybrid multipolar plasmons for 1000-Fold broadband visible fluorescence enhancement and multiplexed biosensing, *ACS Nano* 13 (2019) 13775–13783.
- [25] V. Uzayisenga, X.D. Lin, L.M. Li, J.R. Anema, Z.L. Yang, Y.F. Huang, H.X. Lin, S. B. Li, J.F. Li, Z.Q. Tian, Synthesis, characterization, and 3D-FDTD simulation of Ag@SiO<sub>2</sub> nanoparticles for shell-isolated nanoparticle-enhanced raman spectroscopy, *Langmuir* 28 (2012) 9140–9146.
- [26] S. Zaiba, F. Lerouge, A.M. Gabudean, M. Focsan, J. Lerme, T. Gallavardin, O. Maury, C. Andraud, S. Parola, P.L. Baldeck, Transparent plasmonic nanocontainers protect organic fluorophores against photobleaching, *Nano Lett.* 11 (2011) 2043–2047.
- [27] S. Tang, X. Zhao, L. Yang, B. Li, B. Wang, Copper-catalyzed carboxylation of aryl thianthrenium salts with CO<sub>2</sub>, *Angew. Chem. Int. Ed.* 61 (2022), e202212975.
- [28] J.W. Wang, L. Jiang, H.H. Huang, Z. Han, G. Ouyang, Rapid electron transfer via dynamic coordinative interaction boosts quantum efficiency for photocatalytic CO<sub>2</sub> reduction, *Nat. Commun.* 12 (2021) 4276.
- [29] Y. Magari, T. Kataoka, W. Yeh, M. Furuta, High-mobility hydrogenated polycrystalline In<sub>2</sub>O<sub>3</sub> (In<sub>2</sub>O<sub>3</sub>:H) thin-film transistors, *Nat. Commun.* 13 (2022) 1078.
- [30] S. Yu, P.K. Jain, Plasmonic photosynthesis of C<sub>1</sub>–C<sub>3</sub> hydrocarbons from carbon dioxide assisted by an ionic liquid, *Nat. Commun.* 10 (2019) 2022.
- [31] G. Zhou, T. Li, R. Huang, P. Wang, B. Hu, H. Li, L. Liu, Y. Sun, Recharged catalyst with memristive nitrogen reduction activity through learning networks of spiking neurons, *J. Am. Chem. Soc.* 143 (2021) 5378–5385.
- [32] J. Xu, Z. Ju, W. Zhang, Y. Pan, J. Zhu, J. Mao, X. Zheng, H. Fu, M. Yuan, H. Chen, R. Li, Efficient infrared-light-driven CO<sub>2</sub> reduction over ultrathin metallic Ni-doped CoS<sub>2</sub> nanosheets, *Angew. Chem. Int. Ed.* 60 (2021) 8705–8709.
- [33] Q. Liu, Z. Chen, W. Tao, H. Zhu, L. Zhong, F. Wang, R. Zou, Y. Lei, C. Liu, X. Peng, Edge activation of an inert polymeric carbon nitride matrix with boosted absorption kinetics and near-infrared response for efficient photocatalytic CO<sub>2</sub> reduction, *J. Mater. Chem. A* 8 (2020) 11761–11772.
- [34] H. Ou, G. Li, W. Ren, B. Pan, G. Luo, Z. Hu, D. Wang, Y. Li, Atomically dispersed Au-assisted C-C coupling on red phosphorus for CO<sub>2</sub> photoreduction to C<sub>2</sub>H<sub>6</sub>, *J. Am. Chem. Soc.* 144 (2022) 22075–22082.
- [35] S. Ning, H. Ou, Y. Li, C. Lv, S. Wang, D. Wang, J. Ye, Co<sup>0</sup>·Co<sup>δ+</sup> Interface double-site-mediated C-C coupling for the photothermal conversion of CO<sub>2</sub> into light olefins, *Angew. Chem. Int. Ed.* 62 (2023), e202302253.